ACSNANO

www.acsnano.org

ARTICLE

Directly Visualizing Photoinduced Renormalized Momentum-Forbidden Electronic Quantum States in an Atomically Thin Semiconductor

Hao-Yu Chen, Hung-Chang Hsu, Chuan-Chun Huang, Ming-Yang Li, Lain-Jong Li,* and Ya-Ping Chiu*

Cite This: *ACS Nano* 2022, 16, 9660−9666

Read Online

ACCESS | Metrics & More | Article Recommendations | Supporting Information

ABSTRACT: **Resolving the momentum degree of freedom of photoexcited charge carriers and exploring the excited-state physics in the hexagonal Brillouin zone of atomically thin semiconductors have recently attracted great interest for optoelectronic technologies. We demonstrate a combination of light-modulated scanning tunneling microscopy and the quasiparticle interference (QPI) technique to offer a directly accessible approach to reveal and quantify the unexplored momentum-forbidden electronic quantum states in transition metal dichalcogenide (TMD) monolayers. Our QPI results affirm the large spin-splitting energy at the spin-valley-coupled Q valleys in the conduction band (CB) of a tungsten disulfide monolayer. Furthermore, we also quantify the photoexcited carrier density-dependent band renormalization at the Q valleys. Our findings directly highlight the importance of the excited-state distribution at the Q valley in the band renormalization in TMDs and support the critical role of the CB Q valley in engineering the quantum electronic valley degree of freedom in TMD devices.**

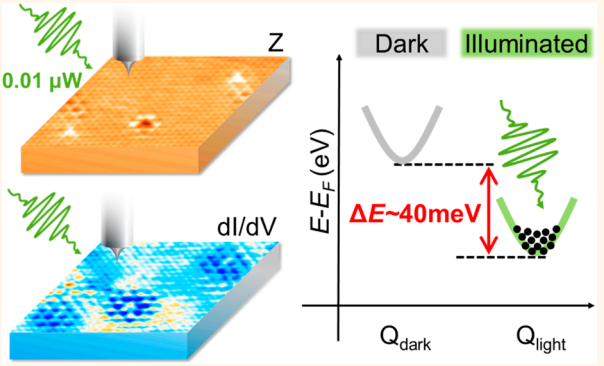

KEYWORDS: *atomically thin semiconductors, transition metal dichalcogenides, momentum degree of freedom, band renormalization, scanning tunneling microscopy, quasiparticle interference technique*

INTRODUCTION

Atomically thin two-dimensional (2D) transition metal dichalcogenides (TMDs), due to their quantum confinement and markedly enhanced electron−electron interactions, have attracted tremendous research interest for their extraordinary transport and optoelectronic properties. In particular, their distinctive spin-valley-coupled band structure provides exotic characteristics with potential applications such as next-generation semiconductors, spin-valleytronic devices, and optoelectronic applications.[1−5] Thus, understanding and manipulating the valley quantum degree of freedom in 2D TMDs will play an important role in future applications.

In 2D TMDs, photoexcitation or hot carrier injection has provided a powerful tool to control the valley degree of freedom.[6,7] The excessive carriers confined in the layered structure of TMDs lead to considerable many-particle interactions.[8−10] This many-body system, bringing the energy renormalization effect and shrinking the quasiparticle bandgap in the valley band structure at the **K** points, has been studied using optical technologies in the past decade.[11,12] Recently, another local minimum of the conduction band (CB) has been noted to lie midway between the **K** and **Γ** points, higher by a few meV than the **K** point, which is called the **Q** valley[13,14] and has been theoretically reported to strongly couple with the **K** valley on the CB edge.[15−17] Intriguingly, the **Q** valley was theoretically predicted to be more sensitive to the energy renormalization effect than the **K** valley due to its differing orbital character and the nonsignificant hole population at the **Q** point.[16] Therefore, the CB **K**-**Q** valley coupling will be dramatically strengthened under the energy renormalization effect with increased carriers, altering the electronic transport

Received: March 26, 2022
Accepted: May 13, 2022
Published: May 18, 2022

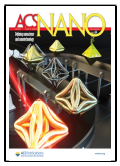

https://doi.org/10.1021/acsnano.2c02981
ACS Nano 2022, 16, 9660−9666

and optoelectronic properties in TMD devices.[18−21] Thus, providing a complete understanding of the underlying physics and developing control of the electronic behavior at the **Q** valley become key to future valleytronic technologies.

To explore the effect of energy renormalization on the energetic band edge position of valley states, an angle-resolved photoemission spectroscopy (ARPES)-based technique is the typical approach used to present the energy renormalization effect via electronic occupied states mapping.[22−25] However, an ARPES-based technique is not a straightforward method for experimentally resolving the momentum-forbidden electronic quantum states at the **Q** valley of atomically thin semiconductors. Capturing the transient hot carrier spreading on the **Q** valley in the femtosecond time-scale before the relaxation to conduction band minimum is challenging due to the signal-to-noise limit and the space-charge effect,[26,27] losing the energy- and momentum-resolution in the ARPES-based technique. In addition, the basic two-photon emission process also restricts the direct evidence to support the energy renormalization effect of the unoccupied states by comparing the intrinsic (nonexcited) and excited conditions. Even though the **K** valley information at CB can be supported by other optical techniques, the clue of the excited-state distribution at the momentum-forbidden **Q** valley state is still lacking, limiting the understanding of the energy renormalization effect at the **Q** valley at CB in the photoexcited TMD systems.

Scanning tunneling microscopy and spectroscopy (STM/S) is a suitable tool for directly probing the atomic surface structure and momentum-sensitive electronic properties in real space, respectively. To further provide information on the above-gap photoexcitation band structure and distinguish spin splitting in the small energy region, quasiparticle interference (QPI) obtained by spatially resolved STS around impurities to offer energy-momentum information has been used to study the electronic band structures in TMD materials in recent years.[28,29] In this work, we present the achievement of combining light-modulated STM and the QPI technique to successfully offer an approach to directly reveal and quantify the unexplored momentum-forbidden electronic quantum states in TMDs.

We obtain direct visualization of the intervalley quantum interference involving the **Q** valleys and affirm the large spin-splitting energy of 240 meV at the **Q** valleys in the CB in atomically thin monolayer tungsten disulfide (WS_2).[28] In addition, we further perform STM/S measurements combined with in situ light illumination to reveal the energy-renormalized **Q** valley with photoexcited charge carriers and the enhanced many-particle interactions in the TMD monolayer. Under above-gap photoexcitation, a downward shift of the quantum electronic state at the **Q** valleys is directly demonstrated in light-modulated QPI patterns. The photoexcited carrier density-dependent energy renormalization at the **Q** valleys is also quantified, with a photoinduced carrier density of approximately 1.2×10^{12} cm^{-2} and a resulting 40-meV downward energy level shift of the **Q** valley under an illumination power of 0.01 μW. Our results significantly highlight the unequivocal presence of spin−valley coupling and the importance of the excited-state distribution at the **Q** valley in the band renormalization in TMDs. This demonstration directly supports that the valley degree of freedom at the **Q** valleys in TMDs can be engineered with light, which is a key figure of merit for future valley-spintronic applications.

RESULT

The growth of monolayer WS_2 (ML-WS_2) by chemical vapor deposition (CVD) on a highly ordered pyrolytic graphite (HOPG) substrate was performed for STM/S measurements in this work. The STM image recorded at a + 1.00 V sample bias in Figure 1(a) shows HOPG and ML-WS_2 terraces with

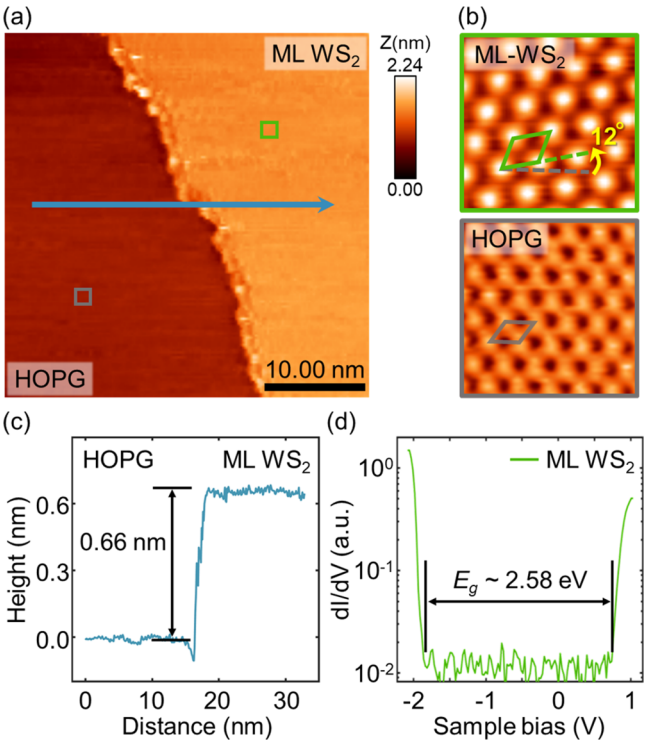

Figure 1. STM topographic image and the spectroscopy of ML-WS_2/HOPG. (a) The STM topographic image recording the HOPG-WS_2 boundary. (Size: 40 × 40 nm^2, sample bias: 1.00 V) (b) The atomic resolution images on HOPG and ML-WS_2 terrace surfaces, showing the difference in the atomic arrangement and the angular misorientation at approximately 12 degrees (Size: 1.5 × 1.5 nm^2 in both pictures) (c) The height alignment refers to the blue arrow in (a) and shows the step with an altitude difference of approximately 0.66 ± 0.02 nm. (d) STS spectrum on the local region of the defect-free ML-WS_2 surface, revealing an energy gap of 2.58 ± 0.02 eV.

different heights. Atomic resolution images of these surfaces are presented in Figure 1(b), showing the difference in the atomic arrangement and an angular misorientation of approximately 12 degrees between HOPG and ML-WS_2 in this region. The height profile in Figure 1(c) across the HOPG-WS_2 boundary, along the blue arrow in Figure 1(a), gives an ML-WS_2 thickness of 0.66 ± 0.02 nm, consistent with previous work.[30] Figure 1(d) shows the differential conductance dI/dV spectrum measured on the ML-WS_2 surface at 77 K. The CB minimum (E_{CB}) and valence band (VB) maximum (E_{VB}) of the ML-WS_2 surface are located at 0.73 ± 0.02 eV and −1.85 ± 0.02 eV, respectively, which yield an electronic energy gap (E_g) corresponding to the sum of the optical bandgap and exciton binding energy of 2.58 ± 0.02 eV for ML-WS_2/HOPG.[31] The general WS_2 optical bandgap is approximately 2.0 eV, leading to an estimated binding energy of 0.58 eV in this work.[32,33] This large binding energy indicates that the ML-WS_2/HOPG system still maintains strong quantum confinement similar to freestanding ML-WS_2 due

https://doi.org/10.1021/acsnano.2c02981
ACS Nano 2022, 16, 9660−9666

to its atomic layered structure. This gives us the opportunity to study the many-particle environment in ML-WS_2, offering energy-momentum-dependent information through STM/S.

Due to the inevitable exposure to the atmosphere before transporting the sample into the UHV environment, the atomically resolved STM image recorded at +0.94 V sample bias (above the CB edge) in Figure 2(a) shows abundant chalcogen-site oxygen substitutional point defects.[31,34] These point defects therefore induce the quantum state scattering process, and to reflect the momentum-related electronic properties of ML-WS_2, QPI measurements are performed. According to previous theoretical support, these point defects are mainly chalcogen-site oxygen substitutional point defects on the top and bottom layers of the sulfur sublattice, $O_s^{(top)}$ and $O_s^{(bottom)}$, respectively, as shown in Figure 2(b).[35] The density of $O_s^{(top)}$ and $O_s^{(bottom)}$ is statistically calculated as 4.3 × 10^{12} cm^{-2} and 2.8 × 10^{12} cm^{-2} in this work, consistent with those in previous works.[36,37] Although chalcogen-site oxygen substitutional point defects are at different geometrical positions in the WS_2 structure, the dI/dV curves in Figure 2(c) show no discrepancy between $Os^{(top)}$ and $Os^{(bottom)}$ in electronic properties. In addition, the corresponding spatially distributed QPI pattern attributed to chalcogen-site oxygen substitutional point defects is presented in Figure 2(d). These spatially distributed QPI patterns, (2 × 2)-like standing waves observed around each defect, can be extracted according to the Fourier transform of the dI/dV image (FT-STS) in Figure 2(e). Obvious spots are observed near the **M** point in the FT-STS map. In addition, the orange-dashed hexagon-like shape in Figure 2(e) outlines the first Brillouin zone (BZ) of WS_2, corresponding to the (2 × 2)-like period around defects in real space. This (2 × 2)-like wave distribution is consistent with previous reports on epitaxial ML tungsten diselenide,[28] in which defect-induced QPI is spin-conserving interference dominated by electron scattering between **Q** valleys. In fact, the Q-Q and Q-K scattering processes are two possible origins of the (2 × 2)-like wave distribution. However, for the parallel momentum ($k_{||}$) in the constant energy contour above the CB of ML-WS_2, the parallel momentum of the states in the Q valley is smaller than that in the K valley.[38] Thus, the tunneling from the electronic states of the K valley decays faster than that of the Q valley, causing the electronic signal from the Q valley to be more significant than that from the K valley in the STM/S measurement. Thus, the QPI pattern in the work is mainly attributed to the Q-Q scattering of ML-WS_2.

ML-WS_2 presents a direct gap at the **K** points and a spin-splitting characteristic at the **Q** point on the CB valley structure, as illustrated by the ML-WS_2 CB edge schematic diagram in Figure 3(a).[39] The spin-splitting characteristic of the ML-WS_2 CB electronic structure is also illustrated in

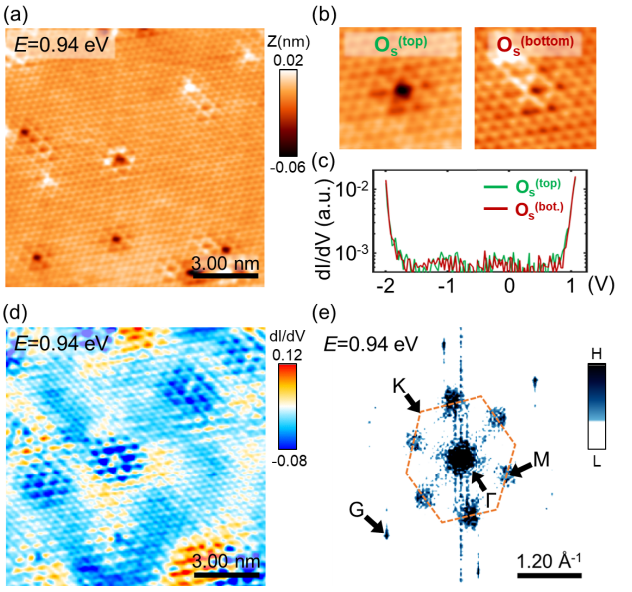

Figure 2. Intervalley quantum interference at oxygen substitutional point defects. (a) The 12 × 12 nm^2 atomically resolved STM images of ML-WS_2 at an energy level of 0.94 eV. (b) The 2.5 × 2.5 nm^2 STM images of the oxygen substituent point defect on the top and bottom layers of the sulfur sublattice, $O_s^{(top)}$ and $O_s^{(bottom)}$, respectively. (c) STS spectra of $O_s^{(top)}$ and $O_s^{(bottom)}$, depicted with green and red lines, respectively. The overlap of these dI/dV curves in (c) shows no discrepancy between $Os^{(top)}$ and $Os^{(bottom)}$ in electronic properties. (d) The STS map corresponds to the scanning region on the topographic picture (a) and reveals the QPI patterns in real space. (e) The 0.94 eV FT-STS map from (d) shows the reciprocal lattice G-point and the QPI patterns around the M-point. The orange dashed hexagon is the first Brillouin zone of ML-WS_2. Obvious spots from the defect-induced QPI pattern are observed near the M point.

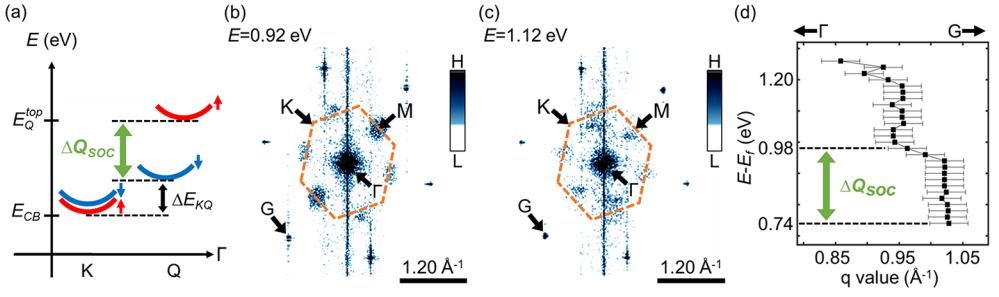

Figure 3. Intervalley quantum interference in the electronic valley structure. (a) The characteristic of the ML-WS_2 CB edge considering spin splitting with a distinct energy interval. The green double arrow indicates ΔQ_{SOC} as the energy difference between the upper and lower subband Q valley minima, and the black double arrow indicates ΔE_{KQ} as the energy difference between the K valley minimum and the lower spin subband Q valley minimum. (b,c) The 0.92 and 1.12 eV FT-STS maps corresponding to the energy level at the lower and upper spin subband Q valleys, respectively. The orange dashed hexagon is the first Brillouin zone of ML-WS_2. The QPI pattern discrepancy between the 0.92 and 1.12 eV FT-STS maps is observed by the location difference between the M-point and the inner first Brillouin zone. (d) The q-value of each QPI pattern extracted from FT-STS maps with an energy interval between 0.70 and 1.26 eV, revealing that the quantity ΔQ_{SOC} of ML-WS_2 is approximately 240 meV.

https://doi.org/10.1021/acsnano.2c02981
ACS Nano 2022, 16, 9660−9666

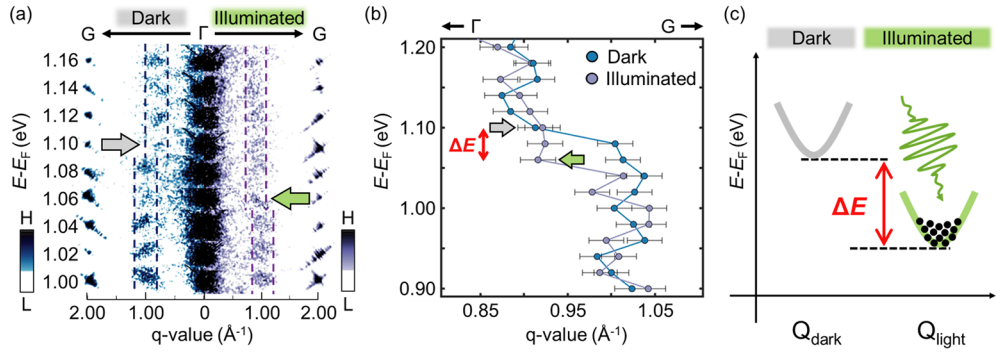

Figure 4. The energy-momentum landscape in the dark and under illumination. (a) The energy-momentum landscape captured along the $\overline{\Gamma G}$ direction from both the dark and illumination FT-STS images with an energy resolution of 20 meV. The energy of the momentum shift is indicated with the gray and green arrows, revealing an energy decline of approximately 40 meV in illumination. (b) The summarized results of the quantized QPI *q*-value in (a), recording each q-value distribution consistently at approximately 0.91 Å^{-1} and 1.01 Å^{-1} in both dark and illuminated conditions. (c) The schematic diagram of the energy renormalization effect on the Q valley due to the many-body interactions from the photoexcited carriers' occupation, leading to the light-induced energy downward shift.

Figure 3(a), where the energy levels $E_Q^{top}$and E_{CB} are the upper spin subband **Q** valley minimum and the CB edge at the **K** valley minimum, respectively. The relationship of the distinct energy interval is given by $E_Q^{top} - E_{CB} = \Delta E_{KQ} + \Delta Q_{SOC}$, where ΔE_{KQ} is the energy difference between the CB edge at the **K** valley minimum and the lower spin subband **Q** valley minimum and ΔQ_{SOC} is the energy difference between the upper and lower subband **Q** valley minima.

Furthermore, according to previous reports,[14] the CB **Q** valley presents a momentum difference between the upper and lower spin subband minima. Comparing the FT-STS maps in Figure 3(b),(c), at energies of +0.92 eV and +1.12 eV above the Fermi level (E_F), the spot in the QPI pattern around the **M** point is preserved at both biases but becomes closer to the center **Γ** point in the FT-STS map at +1.12 eV. Therefore, Figure 3(b),(c) clearly support the momentum shift of the spin-splitting characteristic of the **Q** valley due to the spin−orbit coupling (SOC) effect.[14,28] Moreover, by gradually recording the bias-dependent evolution of the QPI pattern, as shown in Figure 3(d), each *q*-value of the QPI patterns at different biases extracted from the FT-STS results is obtained at a 0.02 eV energy interval. In Figure 3(d), the CB q-value of 1.02 Å^{-1} initially recorded at an energy of +0.74 eV shows the first presence of the QPI pattern at the **M** point, revealing that the energy minimum of the lower spin subband **Q** valley (E_Q^{bottom}) above E_F is +0.74 eV. As the voltage bias continuously increases, the *q*-value shifts from 1.02 to 0.95 Å^{-1}. The momentum shift between the two branches of the **Q** valley spin-splitting characteristic from E_Q^{bottom} = 0.74 eV to E_Q^{top} = 0.98 eV, where $E_Q^{top}$is the energy minimum of the upper spin subband **Q** valley. Therefore, the SOC energy ($\Delta Q_{SOC} = E_Q^{top} - E_Q^{bottom}$) of ML-$WS_2$ at the **Q** valley is found to be approximately 240 meV in this work, confirming the large spin-splitting characteristic at the CB **Q** valley.

To directly examine the photoinduced intervalley quantum interference in **Q** valleys, ML-WS_2 was irradiated *in situ* in light-modulated STM measurements, keeping the same probing region in the dark and under illumination. In addition, the consequent FT-STS images with a 20 meV energy resolution, captured along the $\overline{\Gamma G}$ direction, were sequentially stacked to construct the energy-momentum landscape with the QPI pattern at the **Q** valley, as shown in Figure 4(a). Comparing the results in the dark and under illumination, some points can be mentioned: (1) The diffraction peaks around the **G** point remain at the same position, indicating no laser-induced phase transition under the illumination condition.[40] (2) The blue and purple dashed lines in Figure 4(a) are guides for each *q*-value in the dark and under illumination, respectively. Under both conditions, two branches with a momentum shift due to the spin-splitting characteristic at the **Q** valley are observed. In the present scanning region, we record the occurrence of the momentum shift of E_Q^{top} at +1.10 eV in the dark, as shown in Figure 4(a), which corresponds to the upper subband of the **Q** valley and is indicated by the gray arrow.[14] (3) Under illumination, the energy level E_Q^{top}, labeled with the green arrow, is shifted downward by approximately 40 meV relative to the dark condition. Figure 4(b) maps the momentum (*q*-value) as a function of energy in the light-modulated QPI measurements in Figure 4(a).

DISCUSSION

This work directly compares the momentum-dependent electronic structures in the dark and under illumination to discuss the photophysics of ML TMDs with multiple nearly degenerate CB valleys. Comparing the energy-dependent QPI in the dark and under illumination, shown in Figure 4(b), a light-induced downward energy shift of approximately 40 meV for the upper subband of the **Q** valley is observed in our work. To explicitly explain the energy band downward shift at the **Q** valley in the present experimental results, there are four possible physical mechanisms: (1) the substrate effect, (2) the strain effect, (3) the interlayer interaction, and (4) the enhanced many-body interactions. (1) First, the applied sample bias V = 0 in the STM measurement is aligned to the Fermi level (E_F) of the grounded HOPG substrate. Regarding the substrate effect, under illumination, the photoinduced electron is injected into the conduction band (CB) of WS_2, and the corresponding hole in the valence band (VB) of WS_2 is instantly filled by the electron from the HOPG substrate. In addition, the lifetime of the photoexcited carriers in the CB of WS_2 is shorter than that of holes on the substrate, including the consideration of additional scattering channels.[41,42] This carrier separation behavior thus causes a downshift of the HOPG Fermi level. Thus, under illumination, the energetic CB position of WS_2 is proposed to be away from the E_F of the system at the quasi-equilibrium condition. This

https://doi.org/10.1021/acsnano.2c02981
ACS Nano 2022, 16, 9660−9666

statement is not explicitly consistent with the present experimental observations. Thus, the substrate effect is excluded as the main possible mechanism to explain the downward shift at the **Q** valley in this work.

(2) Next, the second reasonable physical origin could involve optical excitation-induced wrinkling as the strain effect,[43] altering the ML-WS_2 electronic band configuration. However, the lattice reciprocal **G** points in our measurement (see Figure 4(a)) are invariant in their positions under dark and illumination conditions, and the photopulse structural response on the femtosecond time scale is not appropriate for discussions under the quasi-equilibrium condition in STM measurements under continuous-wave laser illumination.

(3) The third reasonable physical origin could be attributed to the moiré domain on the energy renormalization in the Q valley. Energy renormalization has been discussed from the interlayer interaction of twisted TMD bilayers.[44,45] In this kind of twisted TMD systems, the interacting electronic states are above the CB edge. In our present monolayer WS_2/HOPG system, the moiré domain results from the interlayer interaction between the monolayer WS_2 and the HOPG. The interacting electronic states are contributed from the in-gap states below the CB edge of WS_2.[46] Nevertheless, in the present work, the energy renormalized effect is measured and discussed above the CB edge of WS_2. Thus, we suggest that the energy renormalized Q valley in this work is attributed to photoinduced carrier injection instead of the moiré domain. Supporting Information 1 additionally discusses the moiré domain at the below-gap energy level of monolayer WS_2/HOPG in this work.

(4) Therefore, the above exclusions reasonably suggest that we focus on the enhanced many-body interactions induced by photoexcited carrier injection. With above-gap photoexcitation, the carriers transfer between multiple valleys through Coulomb- or phonon-assisted scattering,[47] reaching dynamic equilibration of occupation of the CB **Q** valley, which is schematically depicted in Figure 4(c). Therefore, in such many-body conditions, the classical band structure considering noninteracting electrons is no longer sufficient, and the effect from electron−electron interactions, assembled as the exchange and correlation energy, should be taken into consideration. The challenging exchange-correlation term in many-body problems has been approached by various theoretical approximations,[16,48−50] all indicating a significantly reduced energy with increased carriers in photoexcited TMDs. Thus, the downward energy level shift of the **Q** valley can be attributed to the many-body interactions with photoexcited carriers, leading to band renormalization with a high carrier density under illumination. In this work, a photoinduced carrier density of approximately 1.2×10^{12} cm^{-2} and a resulting 40-meV downward energy level shift of the **Q** valley under an illumination power of 0.01 μW are also quantified.[51] Contrasting with the previous study,[12,23] the giant energy renormalization effect of hundreds of meV from the strong many-particle interactions was only observed in the high carrier density system, crossing over the Mott threshold by the large excitation fluence. Our result with a relatively moderate excitation fluence of approximately ten μJ/s cm^{-2} experimentally confirms that the energy renormalization effect can be effective even below the Mott threshold of 10s of meV, which is also reasonably supported by the theoretical prediction.[52] This finding supports the potential valley-electronic applications of TMDs at the **Q** valley, such as the Mott transition,[12,23] **Q** valley TMD transistors,[53,54] and negative differential conductance.[19,55]

CONCLUSION

In conclusion, the achievement of combining light-modulated STM and the QPI technique to map intervalley quantum interference in a photoexcited TMD monolayer is demonstrated in this work. We obtain a large spin-splitting energy of 240 meV at the CB **Q** valleys on a defective ML-WS_2 surface with abundant chalcogen-site oxygen substitutional point defects. Furthermore, with the light-modulated QPI technique, the direct visualization of the photoexcited carrier occupation indicates an obvious downward energy level shift at the CB **Q** valleys. This result highlights that the CB **Q** valley plays a critical role in engineering the quantum electronic valley degree of freedom in TMD devices by tuning the carrier injection/ejection process. Our findings provide the opportunity to explore the electronic behavior of the valley degree of freedom and the momentum-forbidden electronic quantum states in TMDs for future potential optoelectronic technological applications.

METHODS

For the experiments, we investigated monolayer tungsten disulfide (ML-WS_2) by low-temperature STM (LT-STM) grown on a highly ordered pyrolytic graphite (HOPG) substrate using a typical chemical vapor deposition process (CVD). Tungsten oxide (WO_3, Sigma−Aldrich, 99.995%) powders and HOPG substrate were placed at the center and downstream of the furnace, and sulfur (S, Sigma−Aldrich, 99.99%) powders were placed on the upper stream with another temperature control. During growth, the chamber was kept at 10 Torr and 900 °C (sulfur with 120 °C) for 15 min. Figure 1 shows the different heights, atomic arrangements, and differential conductance dI/dV spectra between the HOPG and ML-WS_2 terraces at 77 K in an ultrahigh vacuum (UHV) environment.

STS measurements were carried out using the lock-in technique (bias modulation δV = 5−10 mV, f = 700−900 Hz). Using this lock-in technique, standard dI/dV vs V spectra as well as topographic differential conductance dI/dV maps for a fixed set voltage were acquired. The latter is used to map the surface LDOS information at the energy corresponding to the set voltage and further obtain the QPI information from each point defect on the ML-WS_2 surface in Figures 2 and 3.

The light-modulated STM setup is the LT-STM combined with an external illumination source at 515 nm and a 0.01 μW continuous-wave laser detected by the power meter. The illuminated area on the ML-WS_2/HOPG is estimated to be approximately 0.1 mm^2, covering the tip scanning region entirely. The excitation fluence per second is calculated as W/A = 10 μ·J/s cm^{-2}, where W is the laser source power and A is the illumination area on ML-WS_2. Based on previous theoretical calculations,[51] an illumination pump fluence of 10 μ·J/s cm^{-2} resulted in a carrier density of approximately 1.2×10^{12} cm^{-2} in this work. Furthermore, the measurement in this work is implemented on the in situ ML-WS_2 surface under both dark and illumination conditions to visualize the photoinduced physics directly in Figure 4.

ASSOCIATED CONTENT

Supporting Information

The Supporting Information is available free of charge at https://pubs.acs.org/doi/10.1021/acsnano.2c02981.

Figure S1(a) shows the atomic topography image of monolayer WS_2 at the in-gap energy level; Figure S1(b) shows the corresponding STS map and the density of states of the moiré domain in S1(a); Figure S1(c) shows the corresponding FT-STS map in S1(b) and displays

https://doi.org/10.1021/acsnano.2c02981
ACS Nano 2022, 16, 9660−9666

the spots of the moiré pattern without the QPI pattern due to the Q-Q scattering process (PDF)

AUTHOR INFORMATION

Corresponding Authors

Ya-Ping Chiu − *Department of Physics and Graduate School of Advanced Technology, National Taiwan University, Taipei 10617, Taiwan; Institute of Physics, Academia Sinica, Taipei 115201, Taiwan; Center of Atomic Initiative for New Materials, National Taiwan University, Taipei 10617, Taiwan;* orcid.org/0000-0001-7065-4411; Email: ypchiu66@ntu.edu.tw

Lain-Jong Li − *Department of Mechanical Engineering, The University of Hong Kong, Hong Kong;* orcid.org/0000-0002-4059-7783; Email: lanceli1@hku.hk

Authors

Hao-Yu Chen − *Department of Physics, National Taiwan University, Taipei 10617, Taiwan*

Hung-Chang Hsu − *Department of Physics, National Taiwan University, Taipei 10617, Taiwan*

Chuan-Chun Huang − *Department of Physics, National Taiwan University, Taipei 10617, Taiwan*

Ming-Yang Li − *Taiwan Semiconductor Manufacturing Company, Hsinchu 30078, Taiwan*

Complete contact information is available at: https://pubs.acs.org/10.1021/acsnano.2c02981

Author Contributions

H.-Y.C. and H.-C.H. contributed equally to this work.

Notes

The authors declare no competing financial interest.

ACKNOWLEDGMENTS

This work was financially supported by the Ministry of Science and Technology (MOST) of Taiwan (Contract No. MOST 109-2628-M-002-005-MY3, MOST 110-2119-M-002-015-MBK, MOST 110-2622-8-002-014), National Taiwan University. (Contract No. NTU-110L7839, NTU-111L7722), and the Center of Atomic Initiative for New Materials, National Taiwan University, Taipei, Taiwan from the Featured Areas Research Center Program within the framework of the Higher Education Sprout Project by the Ministry of Education in Taiwan (111L900802).

REFERENCES

(1) Wang, Q. H.; Kalantar-Zadeh, K.; Kis, A.; Coleman, J. N.; Strano, M. S. Electronics and optoelectronics of two-dimensional transition metal dichalcogenides. *Nat. Nanotechnol.* **2012**, *7*, 699−712.

(2) Chhowalla, M.; Shin, H. S.; Eda, G.; Li, L.-J.; Loh, K. P.; Zhang, H. The chemistry of two-dimensional layered transition metal dichalcogenide nanosheets. *Nat. Chem.* **2013**, *5*, 263−275.

(3) Choi, W.; Choudhary, N.; Han, G. H.; Park, J.; Akinwande, D.; Lee, Y. H. Recent development of two-dimensional transition metal dichalcogenides and their applications. *Mater. Today* **2017**, *20*, 116−130.

(4) Schaibley, J. R.; Yu, H.; Clark, G.; Rivera, P.; Ross, J. S.; Seyler, K. L.; Yao, W.; Xu, X. Valleytronics in 2D materials. *Nat. Rev. Mater.* **2016**, *1*, 16055.

(5) Pei, J.; Yang, J.; Yildirim, T.; Zhang, H.; Lu, Y. Many-body complexes in 2D semiconductors. *Adv. Mater.* **2019**, *31*, 1706945.

(6) Mak, K. F.; Xiao, D.; Shan, J. Light−valley interactions in 2D semiconductors. *Nat. Photonics* **2018**, *12*, 451−460.

(7) Zhao, S.; Li, X.; Dong, B.; Wang, H.; Wang, H.; Zhang, Y.; Han, Z.; Zhang, H. Valley manipulation in monolayer transition metal dichalcogenides and their hybrid systems: status and challenges. *Rep. Prog. Phys.* **2021**, *84*, 026401.

(8) Chernikov, A.; Berkelbach, T. C.; Hill, H. M.; Rigosi, A.; Li, Y.; Aslan, O. B.; Reichman, D. R.; Hybertsen, M. S.; Heinz, T. F. Exciton Binding Energy and Nonhydrogenic Rydberg Series in Monolayer WS_2. *Phys. Rev. Lett.* **2014**, *113*, 076802.

(9) Liu, B.; Zhao, W.; Ding, Z.; Verzhbitskiy, I.; Li, L.; Lu, J.; Chen, J.; Eda, G.; Loh, K. P. Engineering Bandgaps of Monolayer MoS_2 and WS_2 on Fluoropolymer Substrates by Electrostatically Tuned Many-Body Effects. *Adv. Mater.* **2016**, *28*, 6457−6464.

(10) Van Tuan, D.; Scharf, B.; Wang, Z.; Shan, J.; Mak, K. F.; Žutić, I.; Dery, H. Probing many-body interactions in monolayer transition-metal dichalcogenides. *Phys. Rev. B* **2019**, *99*, 085301.

(11) Pogna, E. A. A.; Marsili, M.; De Fazio, D.; Dal Conte, S.; Manzoni, C.; Sangalli, D.; Yoon, D.; Lombardo, A.; Ferrari, A. C.; Marini, A.; Cerullo, G.; Prezzi, D. Photo-Induced Bandgap Renormalization Governs the Ultrafast Response of Single-Layer MoS_2. *ACS Nano* **2016**, *10*, 1182−1188.

(12) Chernikov, A.; Ruppert, C.; Hill, H. M.; Rigosi, A. F.; Heinz, T. F. Population inversion and giant bandgap renormalization in atomically thin WS_2 layers. *Nat. Photonics* **2015**, *9*, 466−470.

(13) Roldán, R.; Silva-Guillén, J. A.; López-Sancho, M. P.; Guinea, F.; Cappelluti, E.; Ordejón, P. Electronic properties of single-layer and multilayer transition metal dichalcogenides MX_2 (M= Mo, W and X= S, Se). *Ann. Phys.* **2014**, *526*, 347−357.

(14) Kormányos, A.; Burkard, G.; Gmitra, M.; Fabian, J.; Zólyomi, V.; Drummond, N. D.; Fal'ko, V. k*p theory for two-dimensional transition metal dichalcogenide semiconductors. *2D Mater.* **2015**, *2*, 022001.

(15) Kaasbjerg, K.; Martiny, J. H.; Low, T.; Jauho, A.-P. Symmetry-forbidden intervalley scattering by atomic defects in monolayer transition-metal dichalcogenides. *Phys. Rev. B* **2017**, *96*, 241411.

(16) Erben, D.; Steinhoff, A.; Gies, C.; Schönhoff, G.; Wehling, T. O.; Jahnke, F. Excitation-induced transition to indirect band gaps in atomically thin transition-metal dichalcogenide semiconductors. *Phys. Rev. B* **2018**, *98*, 035434.

(17) Zhao, P.; Yu, J.; Zhong, H.; Rösner, M.; Katsnelson, M. I.; Yuan, S. Electronic and optical properties of transition metal dichalcogenides under symmetric and asymmetric field-effect doping. *New J. Phys.* **2020**, *22*, 083072.

(18) Sahu, U. K.; Kumar Saha, A.; Gupta, P. S.; Rahaman, H. *In Valley Resolved Current Components Analysis of Monolayer TMDFETs*, 2020 International Symposium on Devices, Circuits and Systems (ISDCS), 2020−03−04; IEEE: 2020; pp 1−5.

(19) Zhang, C.; Cheng, L.; Liu, Y. Understanding high-field electron transport properties and strain effects of monolayer transition metal dichalcogenides. *Phys. Rev. B* **2020**, *102*, 115405.

(20) Schönhoff, G.; Rösner, M.; Groenewald, R. E.; Haas, S.; Wehling, T. O. Interplay of screening and superconductivity in low-dimensional materials. *Phys. Rev. B* **2016**, *94*, 134504.

(21) Piatti, E.; De Fazio, D.; Daghero, D.; Tamalampudi, S. R.; Yoon, D.; Ferrari, A. C.; Gonnelli, R. S. Multi-Valley Superconductivity in Ion-Gated MoS_2 Layers. *Nano Lett.* **2018**, *18*, 4821−4830.

(22) Ulstrup, S.; Čabo, A. G.; Miwa, J. A.; Riley, J. M.; Grønborg, S. S.; Johannsen, J. C.; Cacho, C.; Alexander, O.; Chapman, R. T.; Springate, E.; Bianchi, M.; Dendzik, M.; Lauritsen, J. V.; King, P. D. C.; Hofmann, P. Ultrafast Band Structure Control of a Two-Dimensional Heterostructure. *ACS Nano* **2016**, *10*, 6315−6322.

(23) Liu, F.; Ziffer, M. E.; Hansen, K. R.; Wang, J.; Zhu, X. Direct Determination of Band-Gap Renormalization in the Photoexcited Monolayer MoS_2. *Phys. Rev. Lett.* **2019**, *122*, 246803.

(24) Lee, W.; Lin, Y.; Lu, L.-S.; Chueh, W.-C.; Liu, M.; Li, X.; Chang, W.-H.; Kaindl, R. A.; Shih, C.-K. Time-resolved ARPES Determination of a Quasi-Particle Band Gap and Hot Electron Dynamics in Monolayer MoS_2. *Nano Lett.* **2021**, *21*, 7363−7370.

(25) Bussolotti, F.; Yang, J.; Kawai, H.; Chee, J. Y.; Goh, K. E. J. Influence of many-body effects on hole quasiparticle dynamics in a WS_2 monolayer. *Phys. Rev. B* **2021**, *103*, 045412.
(26) Hellmann, S.; Rossnagel, K.; Marczynski-Bühlow, M.; Kipp, L. Vacuum space-charge effects in solid-state photoemission. *Phys. Rev. B* **2009**, *79*, 035402.
(27) Graf, J.; Hellmann, S.; Jozwiak, C.; Smallwood, C. L.; Hussain, Z.; Kaindl, R. A.; Kipp, L.; Rossnagel, K.; Lanzara, A. Vacuum space charge effect in laser-based solid-state photoemission spectroscopy. *J. Appl. Phys.* **2010**, *107*, 014912.
(28) Liu, H.; Chen, J.; Yu, H.; Yang, F.; Jiao, L.; Liu, G.-B.; Ho, W.; Gao, C.; Jia, J.; Yao, W.; Xie, M. Observation of intervalley quantum interference in epitaxial monolayer tungsten diselenide. *Nat. Commun.* **2015**, *6*, 8180.
(29) Yankowitz, M.; McKenzie, D.; Leroy, B. J. Local Spectroscopic Characterization of Spin and Layer Polarization in WSe_2. *Phys. Rev. Lett.* **2015**, *115*, 136803.
(30) Bradford, J.; Shafiei, M.; Macleod, J.; Motta, N. Synthesis and characterization of WS_2/graphene/SiC van der Waals heterostructures via WO_{3-x} thin film sulfurization. *Sci. Rep.* **2020**, *10*, 17334.
(31) Barja, S.; Refaely-Abramson, S.; Schuler, B.; Qiu, D. Y.; Pulkin, A.; Wickenburg, S.; Ryu, H.; Ugeda, M. M.; Kastl, C.; Chen, C.; Hwang, C.; Schwartzberg, A.; Aloni, S.; Mo, S.-K.; Frank Ogletree, D.; Crommie, M. F.; Yazyev, O. V.; Louie, S. G.; Neaton, J. B.; Weber-Bargioni, A. Identifying substitutional oxygen as a prolific point defect in monolayer transition metal dichalcogenides. *Nat. Commun.* **2019**, *10*, 3382.
(32) Kobayashi, Y.; Sasaki, S.; Mori, S.; Hibino, H.; Liu, Z.; Watanabe, K.; Taniguchi, T.; Suenaga, K.; Maniwa, Y.; Miyata, Y. Growth and Optical Properties of High-Quality Monolayer WS_2 on Graphite. *ACS Nano* **2015**, *9*, 4056−4063.
(33) Jeong, T. Y.; Kim, H.; Choi, S.-J.; Watanabe, K.; Taniguchi, T.; Yee, K. J.; Kim, Y.-S.; Jung, S. Spectroscopic studies of atomic defects and bandgap renormalization in semiconducting monolayer transition metal dichalcogenides. *Nat. Commun.* **2019**, *10*, 3825.
(34) Schuler, B.; Lee, J.-H.; Kastl, C.; Cochrane, K. A.; Chen, C. T.; Refaely-Abramson, S.; Yuan, S.; Van Veen, E.; Roldán, R.; Borys, N. J.; Koch, R. J.; Aloni, S.; Schwartzberg, A. M.; Ogletree, D. F.; Neaton, J. B.; Weber-Bargioni, A. How Substitutional Point Defects in Two-Dimensional WS_2 Induce Charge Localization, Spin−Orbit Splitting, and Strain. *ACS Nano* **2019**, *13*, 10520−10534.
(35) Haldar, S.; Vovusha, H.; Yadav, M. K.; Eriksson, O.; Sanyal, B. Systematic study of structural, electronic, and optical properties of atomic-scale defects in the two-dimensional transition metal dichalcogenides MX_2 (M = Mo, W; X = S, Se, Te). *Phys. Rev. B* **2015**, *92*, 235408.
(36) Rhodes, D.; Chae, S. H.; Ribeiro-Palau, R.; Hone, J. Disorder in van der Waals heterostructures of 2D materials. *Nat. Mater.* **2019**, *18*, 541−549.
(37) Shree, S.; George, A.; Lehnert, T.; Neumann, C.; Benelajla, M.; Robert, C.; Marie, X.; Watanabe, K.; Taniguchi, T.; Kaiser, U. High optical quality of MoS_2 monolayers grown by chemical vapor deposition. *2D Mater.* **2020**, *7*, 015011.
(38) Zhang, C.; Chen, Y.; Johnson, A.; Li, M.-Y.; Li, L.-J.; Mende, P. C.; Feenstra, R. M.; Shih, C.-K. Probing Critical Point Energies of Transition Metal Dichalcogenides: Surprising Indirect Gap of Single Layer WSe_2. *Nano Lett.* **2015**, *15*, 6494−6500.
(39) Zeng, H.; Liu, G.-B.; Dai, J.; Yan, Y.; Zhu, B.; He, R.; Xie, L.; Xu, S.; Chen, X.; Yao, W.; Cui, X. Optical signature of symmetry variations and spin-valley coupling in atomically thin tungsten dichalcogenides. *Sci. Rep.* **2013**, *3*, 1608.
(40) Cho, S.; Kim, S.; Kim, J. H.; Zhao, J.; Seok, J.; Keum, D. H.; Baik, J.; Choe, D.-H.; Chang, K. J.; Suenaga, K. Phase patterning for ohmic homojunction contact in $MoTe_2$. *Science* **2015**, *349*, 625−628.
(41) Aeschlimann, S.; Rossi, A.; Chávez-Cervantes, M.; Krause, R.; Arnoldi, B.; Stadtmüller, B.; Aeschlimann, M.; Forti, S.; Fabbri, F.; Coletti, C.; Gierz, I. Direct evidence for efficient ultrafast charge separation in epitaxial WS_2/graphene heterostructures. *Sci. Adv.* **2020**, *6*, eaay0761.
(42) Fu, S.; Fossé, I. d.; Jia, X.; Xu, J.; Yu, X.; Zhang, H.; Zheng, W.; Krasel, S.; Chen, Z.; Wang, Z. M.; Tielrooij, K.-J.; Bonn, M.; Houtepen, A. J.; Wang, H. I. Long-lived charge separation following pump-wavelength−dependent ultrafast charge transfer in graphene/WS_2 heterostructures. *Sci. Adv.* **2021**, *7*, eabd9061.
(43) Mannebach, E. M.; Li, R.; Duerloo, K.-A.; Nyby, C.; Zalden, P.; Vecchione, T.; Ernst, F.; Reid, A. H.; Chase, T.; Shen, X.; Weathersby, S.; Hast, C.; Hettel, R.; Coffee, R.; Hartmann, N.; Fry, A. R.; Yu, Y.; Cao, L.; Heinz, T. F.; Reed, E. J.; et al. Dynamic Structural Response and Deformations of Monolayer MoS_2 Visualized by Femtosecond Electron Diffraction. *Nano Lett.* **2015**, *15*, 6889−6895.
(44) Förg, M.; Baimuratov, A. S.; Kruchinin, S. Y.; Vovk, I. A.; Scherzer, J.; Förste, J.; Funk, V.; Watanabe, K.; Taniguchi, T.; Högele, A. Moiré excitons in $MoSe_2$-WSe_2 heterobilayers and heterotrilayers. *Nat. Commun.* **2021**, *12*, 7.
(45) Gillen, R.; Maultzsch, J. Interlayer excitons in $MoSe_2$/WSe_2 heterostructures from first principles. *Phys. Rev. B* **2018**, *97*, 165306.
(46) Lu, C.-I.; Butler, C. J.; Huang, J.-K.; Chu, Y.-H.; Yang, H.-H.; Wei, C.-M.; Li, L.-J.; Lin, M.-T. Moiré-related in-gap states in a twisted MoS_2/graphite heterojunction. *npj 2D Mater. Appl.* **2017**, *1*, 24.
(47) Liu, F.; Li, Q.; Zhu, X.-Y. Direct determination of momentum-resolved electron transfer in the photoexcited van der Waals heterobilayer WS_2/MoS_2. *Phys. Rev. B* **2020**, *101*, 201405.
(48) Qiu, D. Y.; Felipe, H.; Louie, S. G. Screening and many-body effects in two-dimensional crystals: Monolayer MoS_2. *Phys. Rev. B* **2016**, *93*, 235435.
(49) Meckbach, L.; Stroucken, T.; Koch, S. W. Giant excitation induced bandgap renormalization in TMDC monolayers. *Appl. Phys. Lett.* **2018**, *112*, 061104.
(50) Faridi, A.; Culcer, D.; Asgari, R. Quasiparticle band-gap renormalization in doped monolayer MoS_2. *Phys. Rev. B* **2021**, *104*, 085432.
(51) Erben, D.; Steinhoff, A.; Lorke, M.; et al. Optical nonlinearities in the excited carrier density of atomically thin transition metal dichalcogenides. 2020, arXiv:2012.07642. arXiv preprint. DOI: 10.48550/arXiv.2012.07642 (accessed 2020-12-15).
(52) Steinhoff, A.; Florian, M.; Rösner, M.; Schönhoff, G.; Wehling, T. O.; Jahnke, F. Exciton fission in monolayer transition metal dichalcogenide semiconductors. *Nat. Commun.* **2017**, *8*, 1166.
(53) Desai, S. B.; Madhvapathy, S. R.; Sachid, A. B.; Llinas, J. P.; Wang, Q.; Ahn, G. H.; Pitner, G.; Kim, M. J.; Bokor, J.; Hu, C.; Wong, H. S. P.; Javey, A. MoS_2 transistors with 1-nanometer gate lengths. *Science* **2016**, *354*, 99−102.
(54) Wu, Z.; Xu, S.; Lu, H.; Khamoshi, A.; Liu, G.-B.; Han, T.; Wu, Y.; Lin, J.; Long, G.; He, Y.; Cai, Y.; Yao, Y.; Zhang, F.; Wang, N. Even−odd layer-dependent magnetotransport of high-mobility Q-valley electrons in transition metal disulfides. *Nat. Commun.* **2016**, *7*, 12955.
(55) He, G.; Nathawat, J.; Kwan, C. P.; Ramamoorthy, H.; Somphonsane, R.; Zhao, M.; Ghosh, K.; Singisetti, U.; Perea-López, N.; Zhou, C.; Elías, A. L.; Terrones, M.; Gong, Y.; Zhang, X.; Vajtai, R.; Ajayan, P. M.; Ferry, D. K.; Bird, J. P. Negative Differential Conductance & Hot-Carrier Avalanching in Monolayer WS2 FETs. *Sci. Rep.* **2017**, *7*, 11256.

https://doi.org/10.1021/acsnano.2c02981
ACS Nano 2022, 16, 9660−9666